RSC Advances

PAPER

View Article Online
View Journal | View Issue

Cite this: *RSC Adv.*, 2025, **15**, 34808

Insight into novel ErMI (M = S, Se) chalcohalide materials for next-generation energy applications

Mohannad Al-Hmoud,[a] Banat Gul,[b] Muhammad Salman Khan, *[ce] Mahmoud AlGharram,[d] Siti Maisarah Aziz,[e] Tariq Al Zoubi[f] and Ashour M. Ahmed[a]

Received 29th July 2025
Accepted 18th September 2025

DOI: 10.1039/d5ra05496f

rsc.li/rsc-advances

The study unveils an inclusive first-principles study of the electronic structure, optical, thermoelectric, and elastic properties of two novel rare-earth chalcohalides, ErSI and ErSeI, through density functional theory with the GGA + *U* approach, which includes spin–orbit coupling to account for strong 4f electron correlations. These systems are both dynamically and mechanically stable, having negative cohesive and formation energies, and fulfill all Born criteria for orthorhombic systems. An investigation of electronic band structure shows that ErSI and ErSeI are spin-polarized direct band gap semiconductors with notable exchange splitting and spin-channel asymmetry. ErSI has a larger band gap and enhanced localization of Er-4f states, whereas ErSeI has more dispersive bands, implying improved carrier mobility. Optical spectra suggest substantial absorption in the UV-visible region, with significant dielectric responses and plasmonic features; ErSI has greater dielectric constants and reflectivity, while ErSeI has higher refractive indices and larger interband transitions. Both materials exhibit negative Seebeck coefficients, indicating dominant n-type behavior. ErSI has a slightly greater figure of merit than ErSeI, due to its superior power factor. Mechanical study indicates that both compounds have equivalent ductility, with ErSeI exhibiting slightly larger elastic moduli, indicating greater mechanical resilience. These results suggest that ErSI and ErSeI are fascinating multifunctional materials with applications in thermoelectric modules, optoelectronics, and spintronic technologies.

1. Introduction

Ternary chalcohalides provide a varied set of potentially useful and fascinating characteristics.[1–3] These ferroelectric narrow band gap semiconductors have a fiber-like linked structure. These ferroelectrics are widely employed in optoelectronics, piezo electronics, and low-pressure sensors. Much research has been conducted on the electrical conductivity of $SbSI_2$ (ref. 4) and SbSeI.[5] A new sonochemical method has been established for the direct synthesis of unique nanocrystalline SbSI.[6] Antimony selenoiodide (SbSeI) belongs to the same category and has been widely researched in recent years.[7,8] However, numerous ternary chalcohalide minerals such as Se, Cl, Br, I, Bi, S, Te, and Sb have been experimentally examined. Several studies have been undertaken to examine the intriguing features, which include excellent stability, ferroelectricity, opticality, and electricality.[9,10] Nitsche *et al.*[11] synthesized SbTeBr, SbTeI, and SbSeI materials and investigated their characteristics. Furthermore, Kichambare *et al.*[12] studied SbTeI, determining the activation energy, energy gap, lattice characteristics, and ionization potentials. Surprisingly, BiTeX (X = Cl, Br, I) are developed and physically built *via* a nanoscale converging method.[13] This work indicated that these semiconductors are formed in triple layers. These investigations have developed procedures for depositing these materials in a few layers, and they provide another approach to all additional Janus-type layered structures. The electronic structure and elastic, vibrational, and piezoelectric features of BiXY monolayers, where X stands for S, Se, Te, and Y for Cl, F, Br, and I, were thoroughly examined by Luo *et al.*[14] The dynamic stability of all the reported BiXY structures has been verified by their vibrational frequency studies at temperatures as high as 600 K. Four distinct Raman-active modes were identified in these monolayers, according to calculations of their Raman spectra. By predicting the elastic parameters, the mechanical behavior within the elastic regime was evaluated. The results showed that the monolayers under consideration are both brittle and flexible. After calculating elastic tensors, piezoelectric coefficients were calculated, revealing that the BiXI versions have out-of-

[a]*Department of Physics, College of Science, Imam Mohammad Ibn Saud Islamic University (IMSIU), Riyadh, 13318, Saudi Arabia*
[b]*National University of Sciences and Technology (NUST), Islamabad, Pakistan*
[c]*Department of Physics, Abdul Wali Khan University, Mardan, 23200, Pakistan. E-mail: salmankhan73030@gmail.com*
[d]*Department of Physics, School of Electrical Engineering and Information Technology (SEEIT), German Jordanian University, Jordan*
[e]*UniSZA Science and Medicine Foundation Centre, Universiti Sultan Zainal Abidin, Gong Badak Campus, 21300 Kuala Nerus, Terengganu, Malaysia*
[f]*College of Engineering and Technology, American University of the Middle East, Kuwait*

plane piezoelectric responses that are significantly greater than those seen in recognized transition metal dichalcogenides (TMDs). Excepting BiTeF, which has a direct energy gap, all BiXY monolayers have indirect band gaps that encompass portions of the visible to infrared light spectrum, with values between 1.07 and 2.42 eV.[14] Analyzing Janus AsSeX monolayers, Cheng *et al.*[15] reported that they were mechanically, thermally, and dynamically stable. AsSeCl was determined to be brittle based on the computed bulk-to-shear modulus ratios (B/G) and Poisson's ratios, while AsSeBr and AsSeI showed ductile properties. Their relative lattice thermal conductivities at room temperature are 1.87 W mK^{-1}, 3.80 W mK^{-1}, and 2.63 W mK^{-1}. To understand the heat transfer approaches, other thermal transport variables such as phase volume, group velocity, scattering rate, and Grüneisen parameter were assessed. The calculated thermoelectric figure of merit values of AsSeCl, AsSeBr, and AsSeI at 700 K for doping with the p-type were 1.55, 0.95, and 1.11, respectively. These results indicate promising thermoelectric performance, especially for AsSeCl and AsSeI.[15] Furthermore, because of the unique features of lanthanide elements, rare-earth (RE)-based chalcogenides continue to garner interest. RE^{3+} cations are hard acids that form bonds with anions that are substantially ionic, much like those made by alkaline earth metals. The outside 5d and 6s orbitals are mainly responsible for these bonds' covalent nature, but the inner 4f orbitals contribute a negligible portion because the outer 5s and 5p electrons shield them. Lanthanide contraction, a result of inadequate shielding of the nuclear charge, happens when the atomic number rises because the 4f orbitals enlarge yet cannot successfully enter the inner electron shells. These compounds' potential for application in nonlinear optical applications is made stronger by their frequently unusual crystal forms. The $Hg_3Se_2Cl_2$ combination, which crystallizes in the T5-$I2_13$ space group, is a potential for nonlinear optoelectronic applications because it exhibits both optical activity and electro-optic impacts.[16–19]

These crystals have special technical and theoretical relevance, with polymorphism being one of their most prominent characteristics.[20,21] $Hg_3Se_2Cl_2$ unique mix of physical and chemical properties, as well as its capacity to change functional parameters during modification, making it appropriate in wide range of applications in holography and information storage devices. $Hg_3Se_2Cl_2$ crystals in nanoparticle form are more appropriate for modern optoelectronics applications. The important structural feature of $Hg_3A_2B_2$ (A = S, Se, Te; B = F, Br, Cl, I) materials is their ability to produce multiple polymorphic variations due to the large conformational capacity of the mercury-chalcogen component, and is the sturdily associated parts.[22] BiSI-based systems have historically underperformed.[23] In 2012, Hahn *et al.* reported that BiChI-based systems were n-type proteins with high absorption spectra.[24] Using density functional calculations, Band discrepancies are the primary cause of BiSI-based devices' subpar performance, noted by Ganose *et al.*,[25] who additionally suggested looking into alternate device architectures to increase efficiency. Materials including n-type BiSeBr, p-type BiSI, and p-type BiSeI were recommended for photo cell applications by the different studies on Bi(III) chalcohalides, and BiSeBr and BiSI have been highlighted as well as viable options for room-temperature radiation detection.[26] Additionally, because of their unique electrical properties, Bi-based oxyhalides (BiOA, where A = Br, Cl, and I) demonstrated high photocatalytic effectiveness in more recent experimental studies.[27]

2. Computational method

The physical properties were calculated by means of the (FP-LAPW) method based on DFT with the WIEN2k package.[28] The energy band gaps predicted with typical approximations, such as the LDA or the GGA, are smaller than observed.[29] The GGA + *U* approach is an important tool for accurately simulating the electronic structure of strongly correlated materials such as ErSI and ErSeI, where traditional generalized gradient approximation (GGA) frequently fails to represent the localized character of Erbium (Er) 4f electrons.[30] ErSI and ErSeI are spin-polarized materials with Er^{3+} cations. Their magnetism is principally caused by unpaired 4f electrons. In GGA computations that do not include a Hubbard *U* correction, these f-states are frequently misplaced near the Fermi level, resulting in inaccurate metallic predictions and magnetic moment underestimates. GGA + *U* introduces an on-site Coulomb interaction term (*U*) to better localize the 4f orbitals, accurately opening a gap and improving the description of magnetic behavior. In ErSI and ErSeI, a suitable *U* value for Er^{3+} normally varies between 4 and 6 eV. However, precise *U* can be fitted based on experimental or higher-level theoretical data. Even after the *U* correction, the spin polarization in both materials remains significant, and the materials favor antiferromagnetic or weakly ferromagnetic alignments depending on the exact structural and exchange interaction characteristics. ErSI and ErSeI crystallize in layered structures, with Er atoms coordinated by S/I and Se/I units, respectively, resulting in environments that increase crystal field splitting and spin–orbit coupling effects. GGA + *U* captures the difference between occupied and unoccupied 4f levels, producing an insulating or semiconducting ground state rather than the inaccurate metallic state anticipated by GGA alone. Using GGA + *U* improves the total magnetic moments per Er ion (about 9 μB per Er^{3+}), indicating the importance of f-electron localization. The increased electronegativity difference between S and I in ErSI results in small changes in band gap size and magnetic exchange channels; GGA + *U* simulations suggest that ErSI frequently has a slightly bigger band gap and stronger f-state localization than ErSeI. Furthermore, the presence of heavy elements such as iodine causes significant spin–orbit coupling, when combined with the GGA + *U* method, must be considered to appropriately describe band splitting and magnetic anisotropy. Without spin–orbit coupling, GGA + *U* still generate an insulating state, but with incorrect predictions of magnetic easy axis and band splitting. To provide a quantitatively precise description of ErSI and ErSeI, spin-polarized GGA + *U* computations with spin–orbit coupling are used. Because of their strong spin polarization, large band gaps, and magnetic anisotropy, ErSI and ErSeI are promising candidates for magnetic semiconductors or

spintronic applications, according to calculations. Their layered structure also allows for tunability under strain or external fields, which GGA + U + SOC (spin–orbit coupling) research suggests could affect their electrical and magnetic properties. In conclusion, GGA + U is required to accurately describe the ground-state physics of spin-polarized ErSI and ErSeI, allowing for realistic predictions of band gaps, magnetic moments, and anisotropic behavior caused by 4f-electron correlations and spin–orbit effects. The thermoelectric properties are evaluated with the semi-classical Boltzmann transport equations using constant relaxation time approximation (CRTA), as employed in BoltzTraP software.[31]

3. Results and discussion

3.1 Structural properties

ErSI have hexagonal structure with a space group $\bar{P}6m2$ (see Fig. 1). Er^{3+} is bound in a trigonal planar shape with three identical S^{2-} and six identical I^{1-} atoms. All Er–S bond lengths are 2.45 Å. S^{2-} is bound in a trigonal planar geometry with three identical Er^{3+} and six identical I^{1-} atoms. I^{1-} is connected with six comparable Er^{3+} and six similar S^{2-}. ErSeI has an orthorhombic $\bar{P}6m2$ space group. The structure is two-dimensional, with one ErSeI sheet compatible in the (0, 0, 1) direction. Er^{3+} is bound to four identical Se^{2-} and two comparable I^{1-} atoms, leading to $ErSe_4I_2$ octahedra that share corners and edges. The corner-sharing octahedral tilt angles are 13°. Er–Se bonds can be smaller (2.76 Å) as well as extended (2.78 Å). The Er–I bond lengths are 3.12 Å. Se^{2-} forms a rectangular seesaw relationship with four Er^{3+} atoms. I^{1-} forms an L-shaped relationship with two comparable Er^{3+} atoms. Our computed lattice constants for ErSI (a = 4.18 Å, b = 5.13 Å, c = 10.12 Å) and ErSeI (a = 4.65 Å, b = 5.54 Å, c = 10.57 Å) are comparable to those reported in 32 and 37, confirming the structural accuracy of our results. The determined cohesive and formation energies of ErSI and ErSeI provide useful details about their respective structural stability and bonding properties. The values of for ErSI and ErSeI were determined as −3.03 and −3.16 (eV per atom) (Table 1), respectively, indicating stable crystal structures and strong internal bonding. But the slightly smaller cohesive energy of ErSeI demonstrates that it has stronger interatomic bonding than ErSI. This difference can be attributed to the substitution of selenium (Se) for sulfur (S), as Se has more atomic radius and higher polarizability, leading to greater orbital overlap and bond strength in the Er–Se interaction than the Er–S bond. Also, our calculated cohesive energies (−3.03 eV per atom for ErSI and −3.16 eV per atom for ErSeI) are comparable to SbSI (−2.75 eV per atom,[32]) and SbSeI (−2.78 eV per atom,[37]), showing these materials consistent energy stability. Similarly,

Table 1 The lattice constants, cohesive energies, formation energies, and band gaps (spin-up) for ErMI (M = S, Se) materials

Materials	a (Å)	b (Å)	c (Å)	E_{coh} eV per atom	E_{form} (eV per f.u)	E_g (eV)
ErSI ($\bar{P}6m2$)	4.18	5.13	10.12	−3.03	−2.94	2.20
ScSI	3.89[c]	5.04[c]		−4.71[c]		2.15[c]
BiSI	4.19[a]		11.02[a]	−2.75[a]		1.93[a]
SbSI	8.60[e]	10.11[e]				2.08[e]
ErSeI ($\bar{P}6m2$)	4.65	5.54	10.57	−3.16	−2.98	3.30
BiSeI	4.27[a]			−2.61[a]		
SbSeI	4.17[d]			−2.78[d]		
SbSeI	8.48[b]	4.07[b]	10.24[b]			
SbSeI	8.79[e]	10.41[e]	4.16[e]	−3.49[c]		
ScSeI	3.95[c]	5.32[c]				

[a] Ref. 32 [b] Ref. 36 [c] Ref. 37 [d] Ref. 38 [e] Ref. 39

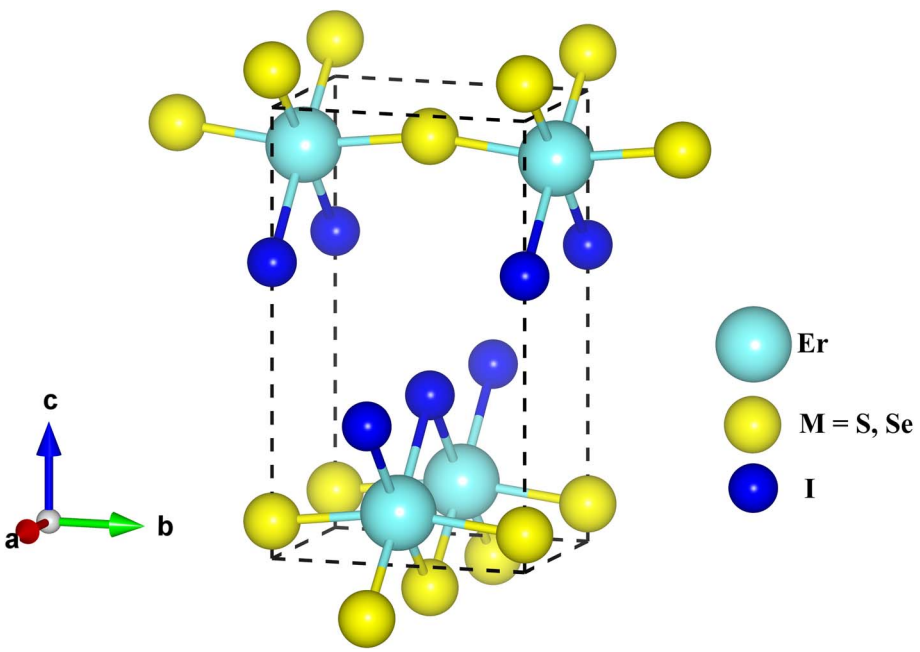

Fig. 1 The optimized crystal structure for ErMI (M = S, Se) materials.

ErSI and ErSeI have formation energies of −2.94 and −2.98 eV per atom, respectively (see Table 1). The formation energy signifies the thermodynamic favorability for producing a compound from its elemental constituents, indicating that ErSeI is slightly more stable than ErSI. This enhanced stability can be related to the more favorable energetics of Er–Se bond formation as compared to Er–S. In terms of component elements, erbium (Er), a lanthanide with a typical +3 oxidation state, is vital for lattice stability due to its strong electrostatic interactions with chalcogen and halogen anions. The S and Se atoms have a significant influence when evaluating the covalency and flexibility of the bonding environment. Se, which is larger and more polarizable than S, promotes improved bonding and lattice stability in ErSeI. Iodine(I), a massive and substantially polarizable halogen, offers ionic character and contributes to lattice stability through strong Er–I interactions. The combined impact of these atomic qualities causes ErSeI to have somewhat stronger bonding and greater thermodynamic stability than ErSI. Fig. 2(a and b) displays the (E–V) relationship for ErSI and ErSeI, providing information on their structural stability and equilibrium volumes. In both circumstances, a classic parabolic curve is observed, which is representative of the energy minimization behavior of crystalline solids: as volume changes, the system's total energy reduces to a minimum before increasing again. The minimum energy for ErSI (Fig. 2(a)) is around 620 atomic units^3 (a.u.^{3}), whereas for ErSeI in Fig. 2(b) it is around 1560 a.u.^{3}. This significant difference in equilibrium volume reflects selenium's higher atomic radius compared to sulfur, resulting in a larger unit cell for ErSeI. ErSI has a lower total energy value (about −41236.636 R_y) than ErSeI (approximately −90266.953 R_y), although direct comparisons of absolute energy values between different materials are often less useful; instead, the focus is on curvature and minima position. A stronger curvature around the minimum indicates a harder material with a higher bulk modulus, whereas a flatter curve implies greater compressibility. Visual inspection reveals that ErSI has a little sharper curve than ErSeI, implying that it is mechanically stiffer and less compressible. This mechanical property difference could have an impact on thermal conductivity, lattice dynamics, and possibly the thermoelectric behavior mentioned before. Overall, these plots show that both materials are structurally stable, but ErSI has a denser, more closely bonded structure, whereas ErSeI is more extended and softer due to the Se substitution for S. This is consistent with prior studies on thermal and electrical transport properties, providing a structural underpinning for the thermoelectric performance variances.

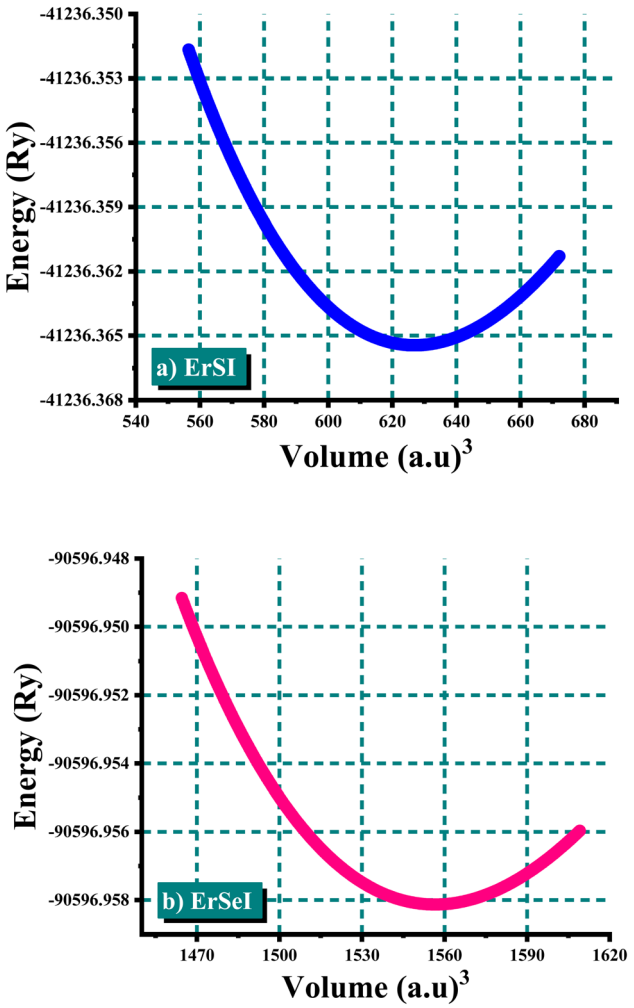

Fig. 2 The energy *vs.* volume optimization plots of (a) ErSI and (b) ErSeI materials.

3.2 Electronic properties

The band structures provided show the electronic properties of ErSI and ErSeI materials calculated using the GGA + *U* method, a density functional theory (DFT) approach that accounts for strong on-site Coulomb interactions, which are frequently required in systems containing localized f-electrons such as Erbium (Er). Fig. 3(a–d) show the electronic structures of ErSI and ErSeI, respectively, with spin-up and spin-down channels presented individually to indicate spin polarization effects. States above the Fermi level (positive energy) are unoccupied conduction bands, and those below (negative energy) are occupied valence bands. Importantly, the (Fig. 3(a) and (c)) depict the spin-up, while the (Fig. 3(b) and (d)) reflect the spin-down case. The arrows show whether the focus is on the conduction band minimum (CBM) (upward arrow) or the valence band maximum (VBM) (downward arrow), which helps to emphasize the dominant carrier type (electrons or holes) in each spin channel. Both ErSI and ErSeI are indirect band gap materials. For ErSI, the band gap values are 2.20 for spin up, whereas for ErSeI, they are 3.30 for up spin. The computed band gaps of 2.20 eV (spin up) for ErSI and 3.30 eV (spin up) for ErSeI are consistent with ScSI (2.15 eV,[37]) demonstrating the accuracy of our electronic structure results. Starting with the ErSI material Fig. 3(a) depicts the spin-up electronic structure. The conduction band minimum (CBM) is near the Fermi level, with a large gap between the valence band maximum (VBM) and the CBM, indicating a semiconducting nature. The bands in the spin-up channel are moderately dispersive, implying that the charge carriers have moderate effective masses, which is

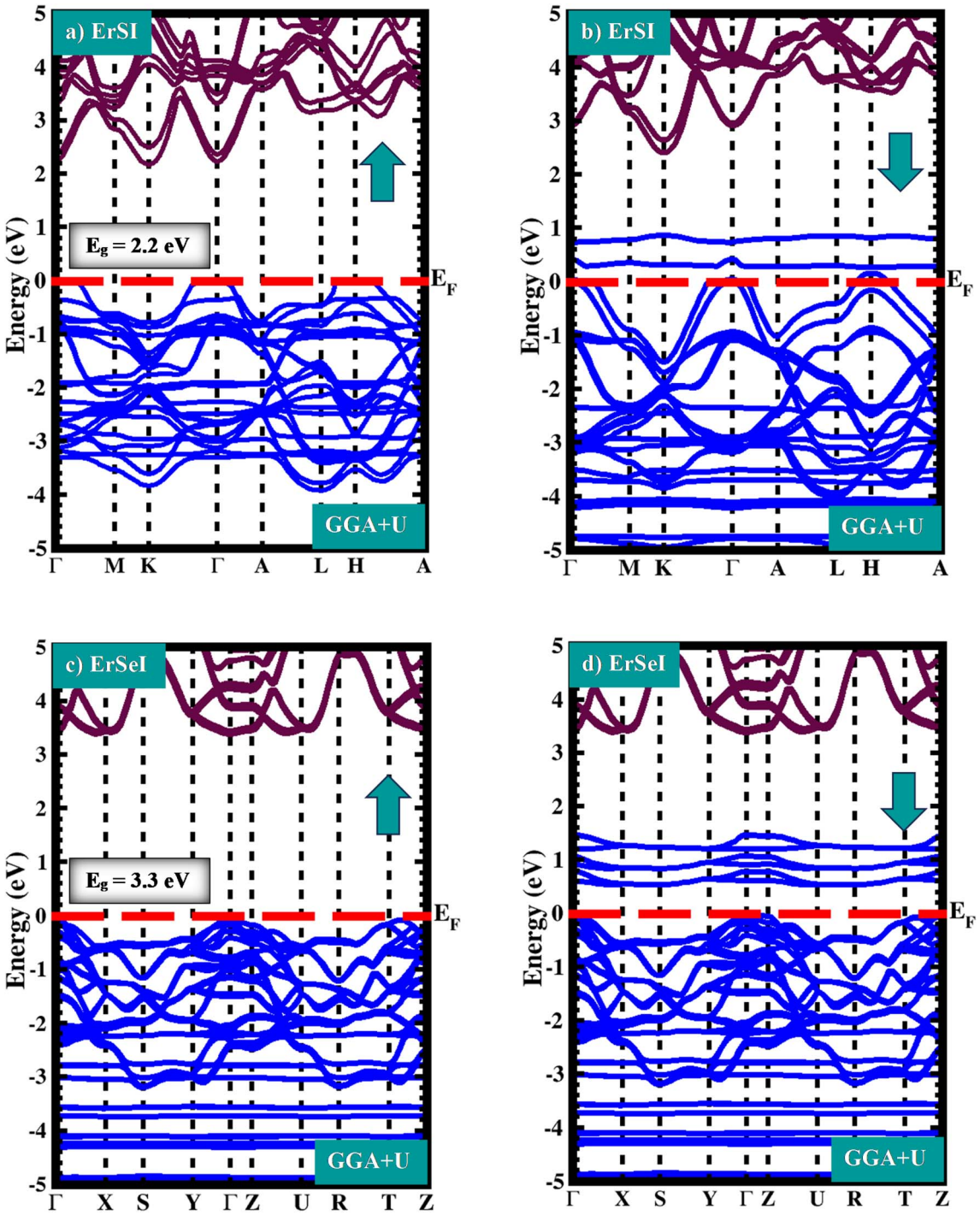

Fig. 3 Spin-polarized electronic band structures of (a and b) ErSI and (c and d) ErSeI computed using GGA + *U*. Panels (a and c) signify the spin-up channel (↑) with band gaps of 2.2 eV for (ErSI) and 3.3 eV for (ErSeI) respectively. Panels (b and d) signify the spin-down channel (↓), where metallic behavior is evident due to the valence band crossing the Fermi level (E_F).

advantageous for increased carrier mobility, a critical attribute for thermoelectric performance. The CBM emerges along the Γ–A direction, and the VBM is relatively flat, indicating a large density of states (DOS) around the Fermi level, possibly enhancing the Seebeck coefficient.

The spin-polarized band profiles of ErSI and ErSeI (Fig. 3(b and d)) show unique metallic behavior in the spin-down channels. In both materials, the valence and conduction bands overlap at the Fermi level (E_F), demonstrating the absence of a band gap and demonstrating metallic conductivity. The crossing of electronic states at E_F implies the presence of delocalized charge carriers that are capable of shifting under an external field, which is typical for metallic systems. ErSI (Fig. 3(b)) has conduction bands that cross E_F, indicating

multiple electron transport paths resulting in a large carrier density. Similarly, in ErSeI (Fig. 3(d)), the spin-down channel exhibits a large overlap of bands at E_F, but with somewhat distinct dispersion properties from ErSI. The metallic behavior in both materials results from the hybridization of Er-4f, transition metal d, and chalcogen p states, which expand around E_F and close the gap in the spin-up states. Such spin-dependent metallicity is particularly interesting since it indicates half-metallic properties, where only one spin channel (spin-down) is metallic and the other remains semiconducting. From a transport perspective, this assures an ongoing availability of transient electrons in the metallic spin-down channel, which improves conductivity and can be used for spin-polarized current input. When comparing the two materials, ErSI has stronger band dispersion near E_F, showing more electron mobility, while ErSeI has relatively flatter bands, reflecting larger carriers but possibly a larger density of states at E_F. This minor distinction shows that, while both materials have metallic spin-down properties, ErSI could encourage faster carrier dynamics, while ErSeI could promote stronger electronic correlations. In general, the metallic behavior of these compounds in the spin-down state is essential to their prospective application in spintronic and conductive device applications. In Fig. 3(c), the spin-up channel exhibits a well-defined band gap, though one that is narrower than that reported in ErSI. The CBM is shown to be of primary relevance (upward arrow), with a conduction band that approaches the Fermi level, implying that electrons can be easily excited into the conduction band at relatively low temperatures. The valence bands are more tightly packed than in ErSI, implying a higher density of states and possibly a larger Seebeck value. Notably, the conduction bands for ErSeI in the spin-up configuration are slightly more dispersive than those for ErSI, implying a trade-off between lower effective mass (greater mobility) and possibly lower Seebeck coefficient.

Comparing ErSI and ErSeI directly offers important information about the influence of anion substitution (S to Se) on electronic characteristics. Because sulfur is lighter and smaller than selenium, it causes slightly wider band gaps in ErSI than ErSeI, which is consistent with chalcogenide family tendencies overall. Furthermore, the substitution increases band dispersion in ErSeI, implying higher carrier mobility than ErSI. A comparison of spin-up and spin-down channels reveals that spin-splitting is more evident in ErSI, particularly near the conduction band, than in ErSeI. This shows that ErSI has stronger magnetic contacts or exchange splitting, which could be due to changes in crystal field effects or hybridization strength between Er-4f and chalcogen p-states. From a materials design standpoint, ErSI's greater band gap suggests it could perform better as a high-temperature thermoelectric material, assuming adequate carrier doping is performed. In contrast, ErSeI's reduced band gap (spin up) suggests that it could operate efficiently at lower temperatures. Furthermore, the effective masses determined from the curvature of the bands demonstrate that ErSeI has more dispersive bands than ErSI, implying potentially higher electronic conductivity. The more localized (flat) valence bands in ErSI indicate lower mobility but higher Seebeck coefficients, emphasizing the delicate balance necessary in thermoelectric design between electrical conductivity and thermopower. The spin polarization seen in both materials points to potential uses outside thermoelectric, such as spintronics, where control over spin channels could lead to novel functions. The asymmetrical shifts between spin-up and spin-down bands point to the prospect of half-metallicity under doping or external strain, with a highly desirable property for spintronic devices. However, neither ErSI nor ErSeI exhibits true half-metallic behavior in the pristine state, as both spin channels have a distinct band gap around the Fermi level.

Fig. 4 shows the density of states, indicating the formation of electronic states. Furthermore, for both spin-up and spin-down orientations, Fig. 4 shows the accurate partial density of states for each atom in the given composition. At the valence band, both materials exhibit Er-4f hybridization (mixing) at a lower energy range. At the Fermi level, Er solely contributes to the spin-down channel. In the conduction band, Er only contributes to the spin-down state at 1.0 eV. The 4f orbitals in rare-earth elements, such as Er, are highly confined and have a small energy range. They are not as widespread as s- or p-states. However, due to crystal field effects (from neighboring atoms such as S, Se, and I) and spin–orbit coupling, these 4f states can split and hybridize slightly with nearby anion p-states (S-3p, Se-4p, or I-5p). Er possesses unpaired 4f electrons, which produce magnetic moments. This separates the 4f bands into spin-up and spin-down channels (exchange splitting). This means that spin-up 4f states are completely occupied and pushed deeper into the valence band, whereas spin-down states are partially occupied and cross into conduction. Because Se is larger and has a different electronegativity than S, the energy hybridization in ErSeI (Fig. 4(b)) is slightly broader or shifted from −5.0 to −3.0 eV against −5.0 to −2.5 eV in ErSI (Fig. 4(a)). The Er 4f spin-down states first arise in the conduction band about 1.0 eV. No spin-up states exist here because, as previously stated, the 4f spin-up states are already fully occupied and have lower energy. The p orbitals of S and Se dominate in both ErSI and ErSeI materials from −3.0 eV to 0 eV. The d states of S and Se have a minor contribution in the CB (4.0 eV). S and Se are chalcogens (group 16). Their p states are naturally situated at lower energies (negative binding energies) and generally fill the valence bands. Sulfur's 3p orbitals are deeper than Se's 4p states because the latter is heavier. S and Se d states have higher energies and are frequently vacant; therefore, there are only minor contributions around 4.0 eV (conduction band). In both spin channels, the I-p orbitals substantially hybridize between −1.8 eV and the Fermi level. At 4.0 eV, the I-p states make up very little of ErSI (Fig. 4(a)). For ErSeI (Fig. 4(b)), the I-p orbitals hybridize up to +1.5 eV (just inside the conduction band). Iodine(I) is a halogen (Group 17), having relatively shallow 5p orbitals (higher energy than S-3p or Se-4p), allowing them to hybridize with Er and S/Se orbitals immediately below and above the Fermi level.

3.3 Mechanical properties

The elastic behaviors of systems are critical when assessing their reliability, performance, and applicability in both

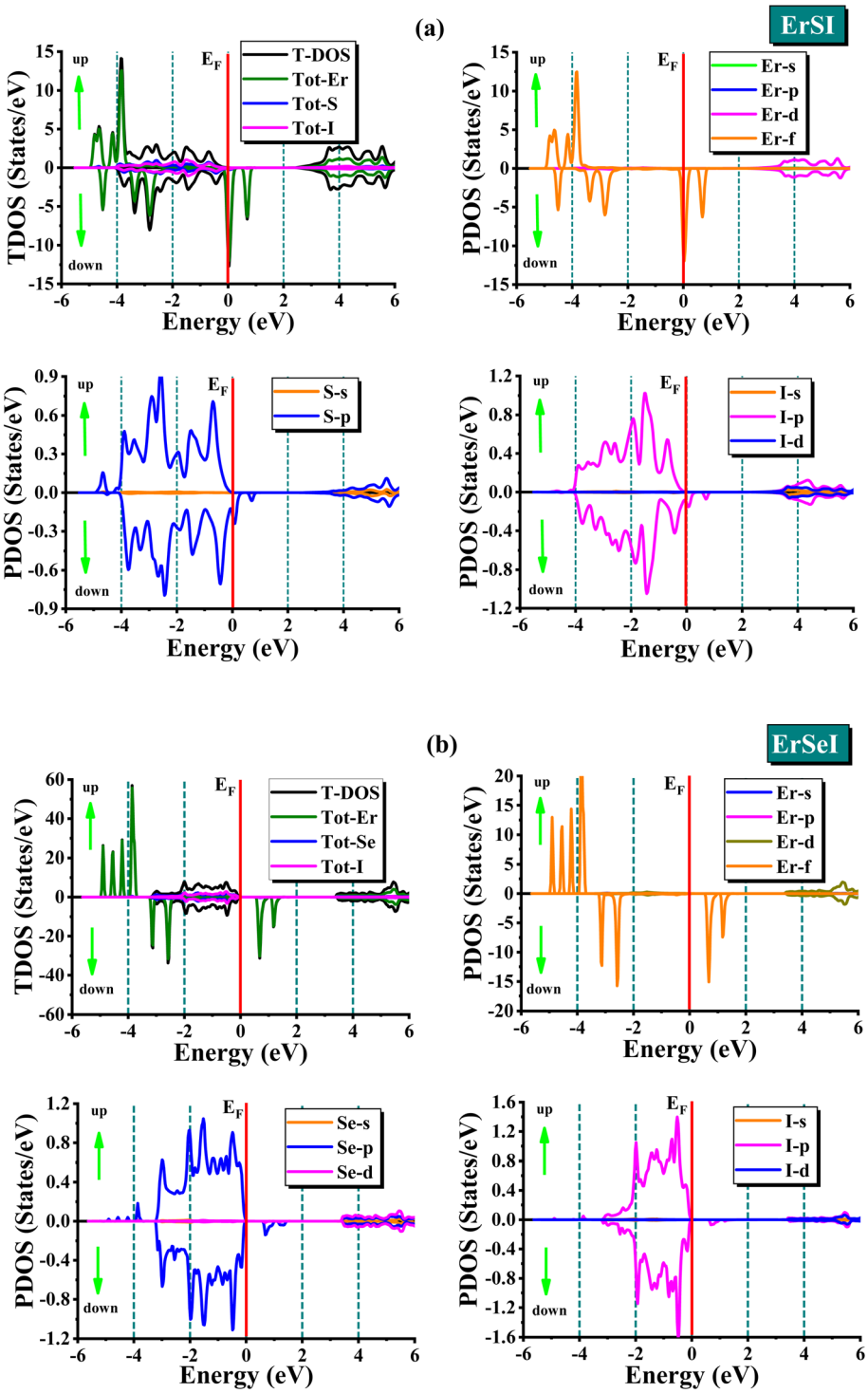

Fig. 4 Spin-polarized total and partial density of states (DOS) of (a) ErSI and (b) ErSeI calculated with GGA + *U*. Spin-up and spin-down channels are indicated by the green arrows in up and downward direction. The vertical dashed line at 0 eV corresponds to the Fermi level (E_F).

fundamental and applied sciences, particularly in optoelectronic, thermoelectric, and spintronic applications. In this context, rare-earth halide chalcogenides such as ErSI and ErSeI, which crystallize in the orthorhombic *Pnma* structure, present an intriguing platform because of their distinctive lattice topologies and bonding properties. A thorough examination of their elastic constants and derived mechanical properties can reveal important information about their bonding strength, anisotropy, ductility, and general mechanical stability. The bulk modulus (B), is slightly higher for ErSI (53.96 GPa) than for ErSeI (51.50) (see Table 2). This small increase indicates that ErSI is slightly more incompressible, probably due to stronger

Table 2 The elastic constants and parameters (such as Bulk modulus (B), Shear modulus G, Young (Y), Poisson's-ratio (ν), Cauchy pressure (C''), Pugh-ratio (B/G), anisotropy constant (A), and Shear constant (C'), for the ErSI and ErSeI materials)

Materials	C_{11}	C_{12}	C_{13}	C_{22}	C_{23}	C_{33}	C_{44}	C_{55}	C_{66}	B	G	Y	ν	C''	B/G	A	C'
ErSI	105.34	69.7	62.34	29.89	19.76	24.56	28.65	27.45	22.56	53.96	16.26	44.14	0.35	41.11	3.17	1.27	17.70
BiSI										42.0[b]	24[b]	60.0[b]	0.26[b]		1.75[b]		
SbSI												36.03[e]	0.27[e]				
ScSI										26.07[e]	14.19[e]		0.37[f]		1.84[e]	0.96[e]	
AsSI												37.44[c]	0.33[c]				
ErSeI	107.89	70.2	68.76	30.25	21.79	25.89	29.56	28.76	23.89	51.50	16.66	45.31	0.36	40.68	3.24	1.27	18.80
BiSeI													0.31[a]				
AsSeI												30.73[c]	0.31[c]			2.81[d]	
SbSeI										26.15[d]	12.47[d]	32.28[d]	0.294[d]		2.09[d]	3.15[e]	
SbSeI										25.78[e]	12.92[e]	33.20[e]	0.29[e]		2.00[e]		
ScSeI													0.35[f]				

[a] Ref. 32 [b] Ref. 33 [c] Ref. 34 [d] Ref. 35 [e] Ref. 36 [f] 37

interatomic contacts. The shear modulus (G), which measures resistance to shape distortion, is additionally somewhat greater in ErSeI (16.66 GPa) than in ErSI (16.26 GPa), though the difference is not significant (see Table 2). This suggests that both materials have relatively similar rigidity at shear stress, implying comparable resilience in shear-dependent applications such as microelectromechanical systems (MEMS) or multi-layer flexible devices. The Young's modulus (Y), which demonstrates stiffness and originates from both B and G, contributes to these findings. ErSeI has a slightly greater Young's modulus (45.31 GPa), whereas ErSI has 44.14 GPa (see Table 2). While the difference is low, it demonstrates a consistent trend: the selenium-based compound is a little stiffer, which correlates to higher B and G values. These moduli suggest that both materials are relatively soft, especially when compared to traditional ceramics or metals, which is consistent with what is anticipated from them as layered, semiconducting compounds. The Poisson's ratio (ν) shows the material's ductility and bonding properties. The results of 0.357 for ErSI and 0.360 for ErSeI indicate a predominance of central interatomic forces and place both materials on the ductile–brittle transition. Both ErSI and ErSeI are regarded as ductile, determined by $\nu > 0.26$ (see Table 2). ErSeI's slightly higher ν could be due to stronger ionic or covalent bonds, demonstrated by its bulk and shear modulus. The Pugh's ratio (B/G) is another key ductility measure. A value higher than 1.75 typically suggests ductile behavior, while lower values signify brittleness. In this scenario, the ErSI and ErSeI had Pugh ratios of 3.17 and 3.24, respectively. These values are significantly higher compared to the ductile threshold, signifying that both compounds are expected to have good ductility, with ErSeI being relatively more ductile. This trend increases ErSeI's attraction for application in flexible electronic devices and applications requiring materials that can withstand mechanical deformation without breaking. The Cauchy pressure ($C'' = C_{12} - C_{44}$) provides a qualitative understanding of bonding characteristics. ErSI has a Cauchy pressure of 41.11 GPa, whereas ErSeI has 40.68 GPa (see Table 2). Positive Cauchy pressure levels are often related to metallic or ductile bonding properties, while negative values suggest prescribed covalent bonding and brittleness. Both materials exhibit substantial positive values here, indicating their ductility and the possibility of metallic-type bonding components, which could result from hybridization between Er-4f and halide/chalcogen orbitals.

The shear constant (C'), calculated as $(C_{11} - C_{12})/2$, indicates the material's resistance to shear in the {100} plane. ErSI has a C' value of 17.79 GPa, while ErSeI's is slightly higher (18.83 GPa). The increased shear constant in ErSeI signifies improved mechanical stiffness, albeit marginal, which could impact its capacity to resist deformation when used in nanostructures or anisotropic strain settings. Mechanical anisotropy, or the directional dependency of mechanical reaction, is an important consideration when evaluating the material's performance under practical conditions. The anisotropy constant (A), calculated as $A = 2C_{66}/(C_{11} - C_{12})$, is found to be 1.27 for ErSI and ErSeI, which are virtually identical. A value of $A = 1$ suggests isotropy, while any variation displays growing anisotropy. While both materials exhibit moderate anisotropy, the proximity of these values indicates that ErSI and ErSeI behave identically in terms of directional elasticity, as is anticipated for isostructural compounds where the only significant change is the chalcogen substitution (S *vs.* Se). In combination, this mechanical includes demonstrate that ErSI and ErSeI have equivalent elastic behavior, with ErSeI continually showing slightly higher values for most critical parameters' bulk modulus, shear modulus, Young's modulus, and ductility indicators. These differences, however, are not significant, but are important when choosing materials for specific mechanical performance objectives. For example, ErSeI's superior stiffness and ductility make it a better contender for applications requiring a balance of flexibility and structural integrity, including thermoelectric modules, flexible transistors, and hybrid optoelectronic systems. Meanwhile, ErSI, despite being slightly softer and less ductile, still perform well in low-strain situations or if its distinctive optical or magnetic properties are more important than mechanical endurance. Table 2 in the revised manuscript reveals that our Young's modulus values, the Poisson's ratios, the Cauchy pressure and the B/G ratios agree well with SbSeI ([35]), and are likewise comparable to known values for SbSeI[35] and ScSeI.[37] Furthermore, both ErSI and ErSeI exhibit

mechanical stability because they match the Born–Huang standards for orthorhombic crystals. All of the essential elastic constants are positive and satisfy the essential inequalities, showing their thermodynamic and mechanical robustness. This stability is essential for future investigations into their thermal conductivity, electronic band structure, and possibly topological or magnetic characteristics. Finally, this comparative elastic analysis of ErSI and ErSeI shows that both materials are mechanically stable, ductile, and mildly anisotropic orthorhombic semiconductors. While they share many structural characteristics, ErSeI exceeds ErSI in terms of mechanical performance, with slightly higher resistance to deformation, better ductility, and greater stiffness. These properties distinguish ErSeI as a potential material for future applications in flexible electronics, low-dimensional devices, and dynamically resistant semiconductor technologies. Still, ErSI remains an acceptable option in applications where slightly softer mechanical strength is desirable or when sulfur's chemical characteristics are useful. This investigation underlines the significance of elastic parameter evaluation in choosing and optimizing modern materials to fulfill particular functional applications.

3.4 Optical properties

The real dielectric function, $\varepsilon_1(\omega)$, indicates how a material is polarized in response to an electric field at a specific frequency ω. It has a direct relationship with the material's ability to store energy. Fig. 5(a) illustrates the real dielectric function $\varepsilon_1(\omega)$ for ErSI and ErSeI. ErSI and ErSeI have static dielectric constants $\varepsilon_1(0)$ of 12.0 and 4.5, respectively. ErSI has significantly higher polarizability than ErSeI, which could be due to changes in their atomic structure, bond strength, or how quickly electrons can shift around the atoms. Near 4.0 eV, there is a large density of allowed electronic transitions from occupied to empty electronic states, making the material extremely polarizable at that photon energy. As a result, $\varepsilon_1(\omega)$ increases and peaks at 4.0 eV in both materials. Absorption becomes strong above 4.0 eV, when electrons absorb energy and shift into high-energy states. The significant absorption is mirrored in the imaginary component $\varepsilon_2(\omega)$, which becomes huge. Kramers–Kronig relations in optics link $\varepsilon_1(\omega)$ and $\varepsilon_2(\omega)$, so when $\varepsilon_2(\omega)$ increases due to absorption, $\varepsilon_1(\omega)$ must decrease. At higher energies, electrons can no longer coherently follow the oscillating electric field. Instead of polarizing, the material dissipates energy (absorbs light),

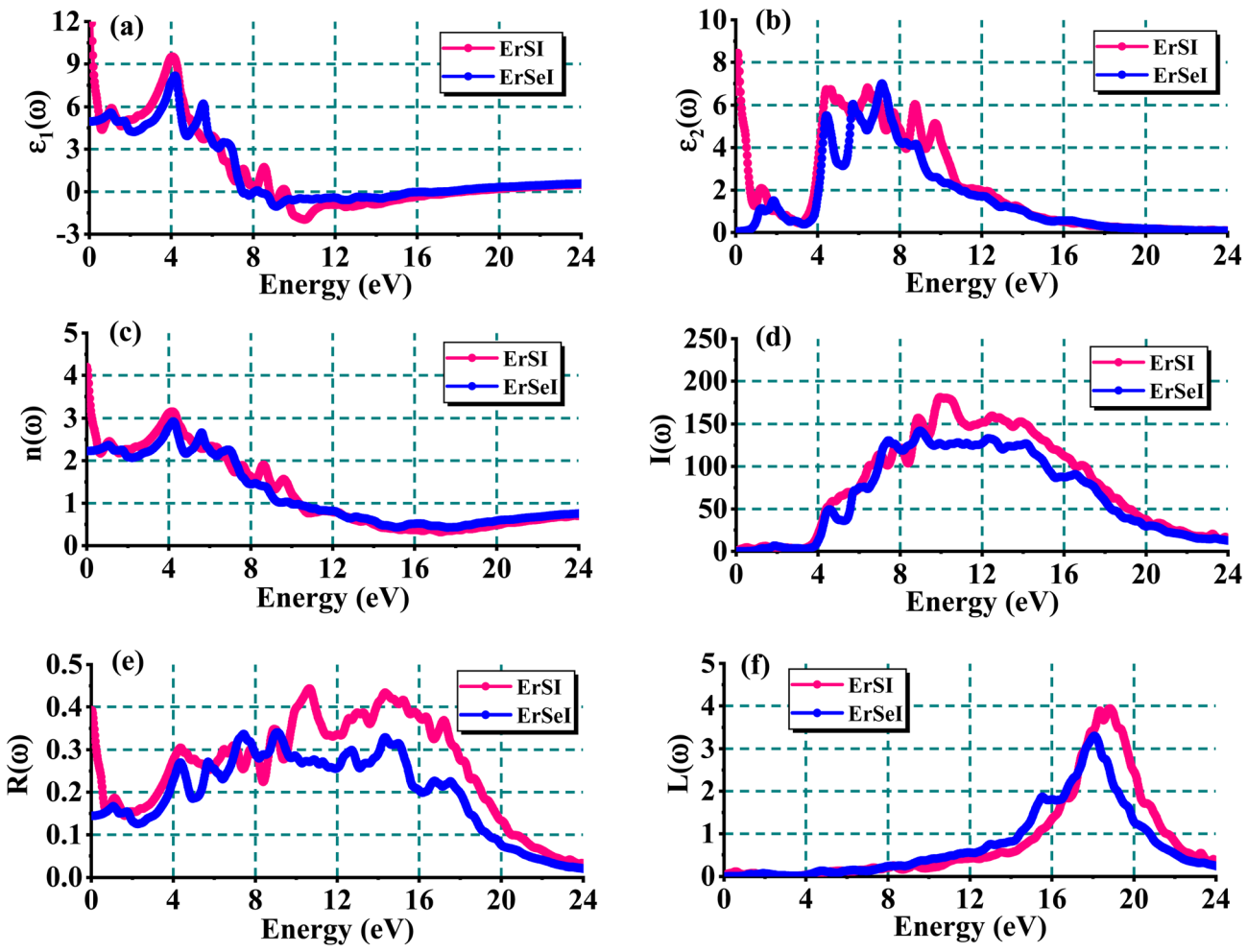

Fig. 5 The computed (a) real dielectric constant, (b) imaginary dielectric constant, (c) refractive index, (d) absorption coefficient, (e) reflectivity, and (f) energy loss function for ErMI (M = S, Se) materials.

reducing the "stored" energy associated with $\varepsilon_1(\omega)$. Fig. 5(b) demonstrates the imaginary dielectric function $\varepsilon_2(\omega)$ for ErSI and ErSeI. The $\varepsilon_2(\omega)$ is directly related to optical absorption. It measures how much light a material can absorb at a given photon energy ($\hbar\omega$) by pushing electrons from occupied to unoccupied electronic states. When $\varepsilon_2(\omega)$ is large, it indicates substantial absorption, which is generally caused by interband electronic transitions (electrons moving from the valence to the conduction band). The largest peak in $\varepsilon_2(\omega)$ for ErSI is at 4.2 eV, while for ErSeI it is at 7.5 eV. The peaks in $\varepsilon_2(\omega)$ indicate high joint density of states (JDOS) and strong optical transition matrix elements at specific energies. This frequently occurs at specific locations in the band structure (for example, transitions between the valence band maximum (VBM) and conduction band minimum (CBM), or between deeper valence bands and higher conduction bands). At very high photon energies, you can begin to study deep core or continuum states in which optical transitions are significantly weaker or banned. As a result, the absorption gets weaker and the imaginary component $\varepsilon_2(\omega)$ diminishes.

The static refractive index n(0) corresponds to the material's electronic polarizability at zero frequency. ErSeI has a higher n(0) of 4.2 than ErSI 2.3 because selenium (Se) is bigger and more polarizable than sulfur (S). More polarizable atoms, such as Se, cause the electron cloud to deform more easily when an electric field is applied, resulting in a higher dielectric constant and hence a higher refractive index at low frequencies. As the photon energy increases, electronic changes (such as interband transitions) occur. After these strong electronic transitions, the material begins to absorb more energy (higher $\varepsilon_2(\omega)$), leading to a fall in $\varepsilon_1(\omega)$. As a result, $n(\omega)$ starts to decline. Furthermore, at high energies, the material becomes increasingly transparent to high-energy photons (beyond specified absorption thresholds), while the refractive response lessens. Fig. 5(d) displays the spectra of the $I(\omega)$ for ErSI and ErSeI. The higher the number of permissible transitions and available electronic states (high joint density of states), the greater the absorption. ErSI and ErSeI exhibit maximum absorption coefficient $I(\omega)$ spectra at photon energies of 10.0 and 9.0 eV, respectively. The combined density of states is high, and strong transitions occur, resulting in a peak in absorption. Beyond 10.0 eV, both materials' absorption coefficient $I(\omega)$ spectra diminish. At very high energies, the conduction band structure of materials such as ErSI and ErSeI become more dispersive (electrons behave more freely as if they were in a metal), reducing optical absorption because transitions become less likely throughout a broad energy range.

Fig. 5(e) displays the static reflectance $R(\omega)$ for ErSI and ErSeI materials. A material's reflectivity $R(\omega)$ is heavily influenced by its electrical structure, specifically how it interacts with photons of varying energy. Reflectivity at zero energy is proportional to the density of free carriers and the material's plasma frequency. ErSI has a higher static reflectivity of 0.4, signifying more free carriers and a stronger polarization response at low frequencies than ErSeI, which is 0.15. These electronic transitions generate a rise in reflectance, which peaks at certain energies. The main peaks for ErSI and ErSeI are 11.0 and 9.5 eV, respectively. The peak positions are related to the critical points in the band structure where many electronic states contribute to optical transitions. As a result, there are fewer transitions, and the material can no longer effectively reflect light, resulting in a drop in reflectivity ($R(\omega)$). Fig. 5(f) displays the energy loss function $L(\omega)$ of ErSI and ErSeI materials. The energy loss function reflects the loss in energy by rapid electrons when they move through a material, indicating areas where the material absorbs energy strongly. Peaks in $L(\omega)$ occur when the $\varepsilon_1(\omega)$ approaches zero and the $\varepsilon_2(\omega)$ is modest but not zero. This circumstance indicates a bulk plasmon resonance, which is a collective oscillation of free or loosely bound electrons at a specific frequency. So, at 19.0 eV for ErSI and 18.0 eV for ErSeI, the materials' electrons collectively oscillate most vigorously, resulting in the greatest energy loss. After the plasmon resonance (the peak), the material no longer allows for intense collective oscillations. The real portion $\varepsilon_1(\omega)$ becomes positive again, indicating that the material acts more like a regular dielectric without considerable absorption from collective modes. $L(\omega)$ decreases as fast electrons interact less strongly with the material, resulting in decreased energy loss. Also, at higher energies, the excitation shifts to individual interband transitions (electron excitations between bands) rather than collective electron oscillations, resulting in decreased intensity in the loss function.

3.5 Thermoelectric properties

The rise in electrical conductivity, as illustrated in Fig. 6(a), is described by the fundamental principles of charge carrier behavior in semiconductors or narrow-gap materials. At 50 K, the thermal energy available to the system is limited. In such cases, fewer electrons have enough energy to be thermally stimulated over the band gap from the valence bands to the conduction bands. As a result, the carrier concentration (electrons in the conduction band or holes in the valence band) remains low, leading to poorer electrical conductivity. At 50 K, the σ/τ values are relatively low: 2.20×10^{18} $(\Omega\ \mathrm{ms})^{-1}$ for ErSI and 2.14×10^{18} $(\Omega\ \mathrm{ms})^{-1}$ for ErSeI. As the temperature rises, more thermal energy becomes accessible. This increased energy allows for greater excitation of electrons across the band gap, which results in a higher concentration of free charge carriers (electrons or holes). The σ/τ is a proxy for σ divided by the scattering time τ; the rise in carrier concentration dominates the behavior, resulting in an overall increase in σ/τ with temperature. The primary cause is thermal excitation of charge carriers. At elevated temperatures, ErSI and ErSeI behave similarly to intrinsic semiconductors, with significant intrinsic carrier production due to thermal activation. In intrinsic conduction, the number of electrons and holes grows exponentially with temperature, considerably increasing conductivity. ErSI consistently exhibits somewhat higher σ/τ values than ErSeI across all temperatures. This shows that ErSI has a slightly higher carrier concentration or mobility. It could also be owing to ErSI's somewhat narrower band gap, which allows for simpler excitation of carriers at lower energy than ErSeI, resulting in better conductivity. At 650 K, the maximal σ/τ values

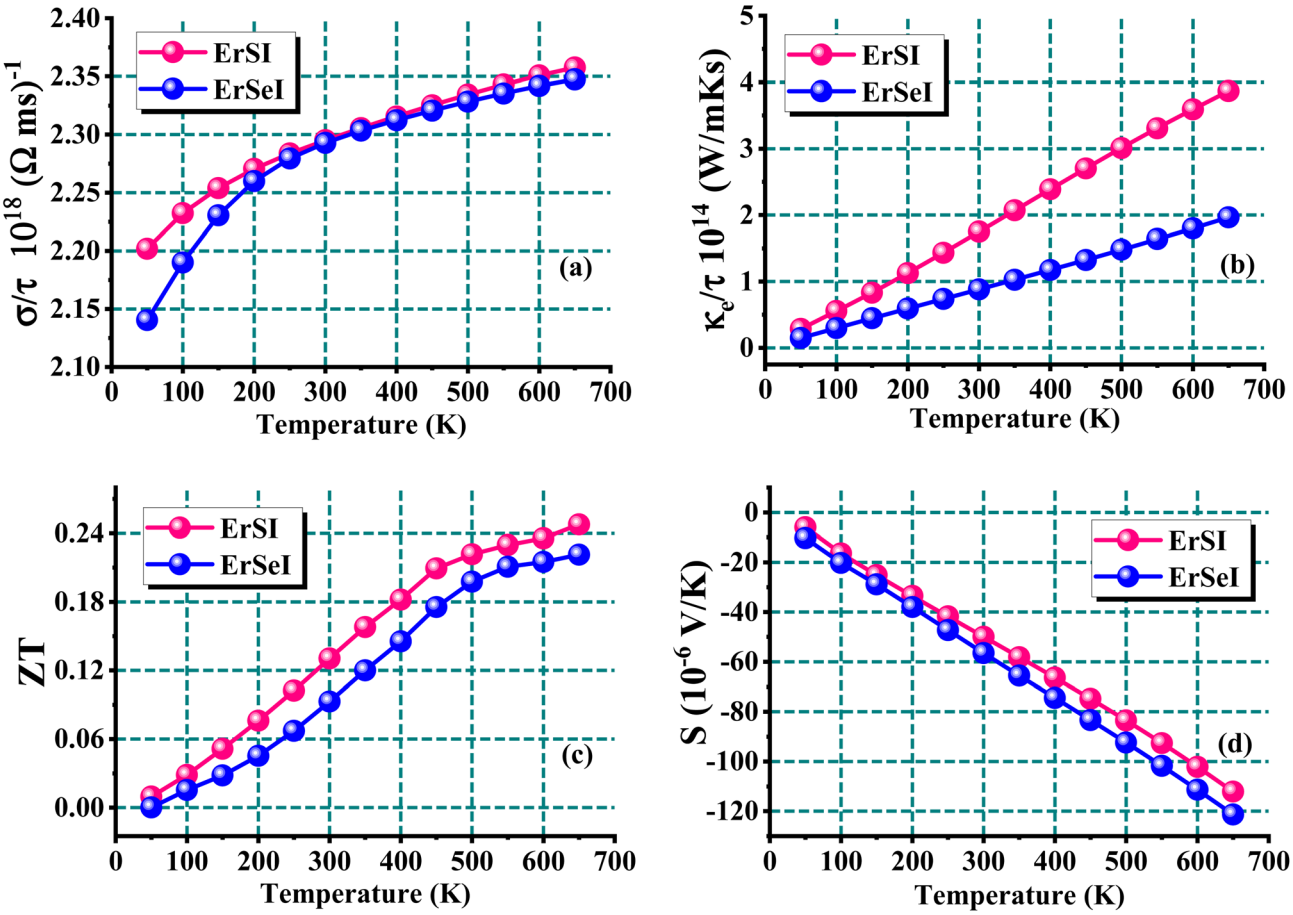

Fig. 6 The computed (a) electrical conductivity, (b) thermal conductivity, (c) figure of merit, and (d) Seebeck coefficient, for ErMI (M = S, Se) materials.

for ErSI (2.36×10^{18}) and ErSeI (2.34×10^{18}) are nearly identical. This suggests that, while ErSI and ErSeI have structural and electrical differences (as seen in the volume and energy charts above), their charge transport properties are roughly similar, with ErSI regularly outperforming ErSeI. The increase in thermal conductivity (κ_e) seen in Fig. 6(b), was attributed to a major role of the electronic thermal conductivity, as well as its dependency on the quantity of charge carriers and their transport characteristics. To begin, a material's thermal conductivity is typically divided into two components: lattice thermal conductivity (κ_l) from phonons (atomic vibrations) and electronic thermal conductivity (κ_e) from charge carriers (electrons or holes). Because thermally excited charge carriers are few in semiconductors and thermoelectric materials at low temperatures, the lattice contribution frequently takes precedence. However, when the temperature rises, the contribution of electrons becomes more important, particularly in narrow-gap semiconductors or materials with higher intrinsic carrier concentration. This equation demonstrates that electronic thermal conductivity rises with both electrical conductivity and temperature. As the temperature rises, more charge carriers are thermally stimulated across the band gap, increasing electrical conductivity (σ), as previously mentioned. Since κ_e is proportional to σ, increasing carrier density results in a greater κ_e. At 300 K, ErSI exhibits a higher thermal conductivity (1.8×10^{14} W m^{-1} K^{-1} s^{-1}) than ErSeI (1.0×10^{14} W m^{-1} K^{-1} s^{-1}), similar to the observed trend in electrical conductivity. This implies that ErSI has either higher carrier concentration, higher carrier mobility, or a smaller effective mass, resulting in improved charge (and consequently heat) transmission *via* carriers. At 600 K, ErSI exhibits higher maximum thermal conductivity (4.0×10^{14} W m^{-1} K^{-1} s^{-1}) than ErSeI (2.0×10^{14} W m^{-1} K^{-1} s^{-1}). If phonon (lattice) thermal conductivity was dominant, it would be expected to decrease as temperature increased due to higher phonon–phonon scattering (Umklapp processes). However, as κ_e increases, it suggests that the electronic contribution takes precedence over the lattice part in the temperature range examined, particularly above 300 K.

The figure of merit (ZT) for ErSI and ErSeI, shown in Fig. 6(c). The increase in ZT with temperature for both ErSI and ErSeI can be attributed to the synergistic effect of rising electrical conductivity (σ) and thermal conductivity (κ_e), as well as the involvement of the Seebeck coefficient. As revealed (see Fig. 6(a)), both ErSI and ErSeI display a rise in the electrical conductivity. As σ appears in the numerator of the ZT formulation, its increase naturally pushes ZT higher, improving power factor ($S^2\sigma$) and thermoelectric performance. Fig. 6(d) indicates that the Seebeck coefficient S gets increasingly negative as

temperature rises, which is characteristic of semiconductors: as temperature rises, the carrier concentration increases, resulting in a fall in S magnitude. However, in ErSI and ErSeI, S does not decrease strongly enough to outweigh the increase in σ. The total effect on $S^2\sigma$ remains positive because the gain in σ is significant enough to exceed the loss in S, leading to an increase in the power factor with temperature. Although electronic thermal conductivity ke improves with temperature (as illustrated in Fig. 6(b)), total thermal conductivity k does not increase significantly enough to cancel out the improvement in $S^2\sigma$. Since ZT is inversely proportional to κ_e, a minor increase in κ_e combined with a substantial increase in $S^2\sigma T$ leads to an overall rise in ZT. ZT is related to temperature (T), which leads to its rise as the system warms. Direct proportionality implies that ZT grows linearly with T, even if other variables (such as $S^2\sigma$ and $1/k$) remain constant. In actuality, when $S^2\sigma$ improves and κ_e increases gradually, ZT rises faster than linearly. ErSI consistently produces slightly higher ZT values than ErSeI (0.12 *vs.* 0.10 at 300 K and 0.24 *vs.* 0.22 at 650 K). ErSI has stronger electrical conductivity and slightly better Seebeck coefficient behavior than ErSeI, which accounts for its superior performance. Furthermore, ErSI has a greater $S^2\sigma$ ratio compared to ErSeI, resulting in higher total thermoelectric efficiency. The greatest ZT values observed at 650 K (0.24 for ErSI and 0.22 for ErSeI) indicate that these materials become more efficient thermoelectric converters as temperatures rise. However, the moderate absolute values of ZT suggest that, while ErSI and ErSeI show promise, greater tuning (such as doping, alloying, or nanostructuring) is required to compete with the best thermoelectric materials. The Seebeck coefficient (S) indicates how much voltage is created per unit temperature variation across the material. The negative sign of the S specifies that electrons were the primary charge carriers (n-type conduction). At low temperatures (50 K), very few carriers are thermally stimulated over the band gap due to the low thermal energy. At 50 K, ErSI and ErSeI had maximal Seebeck coefficients of -5.0×10^{-6} V K^{-1} and -10.0×10^{-6} V K^{-1}, respectively, as shown in Fig. 6(d). This increasing carrier concentration reduces the Seebeck coefficient in common metals and severely doped semiconductors. However, for a semiconductor or small-gap material, the Seebeck coefficient often increases in magnitude (becomes more negative) when the energy-dependent conductivity steepens. At higher temperatures, phonon scattering (scattering caused by lattice vibrations) gets stronger. At 650 K, ErSI and ErSeI have minimal Seebeck coefficients (S) of -118.0×10^{-6} V K^{-1} and -122.0×10^{-6} V K^{-1}, respectively.

4. Conclusions

In conclusion, we executed a DFT-based investigation of ErSI and ErSeI chalcohalides, showing an intriguing interaction of their electronic, optical, thermoelectric, and mechanical properties, demonstrating their potential for multifunctional applications. Both materials are stable in structure, with negative formation and cohesive energies, and are mechanically stable from the Born–Huang criterion. Based on the elastic constant study, ErSeI continuously has a slightly greater shear (16.66 GPa), and Young's modulus (45.31 GPa) compared to ErSI, indicating slightly higher stiffness and incompressibility. Both materials are highly ductile, as revealed by high Pugh's ratios (3.17 for ErSI, 3.24 for ErSeI) and Poisson's ratios (>0.35), and positive Cauchy pressures indicate metallic-like bonding due to orbital hybridization. These properties render ErSeI more mechanically flexible and excellent for flexible thermoelectric or optoelectronic systems that require structural durability. Electronically, both materials are indirect spin-polarized semiconductors that exhibit substantial spin asymmetry; ErSI shows greater exchange splitting, while ErSeI reveals greater band dispersion, implying increased carrier mobility. Optically, the two materials show noteworthy absorption in the visible-UV region, and ErSI possesses more polarizability and reflectivity, and ErSeI has redshifted absorption edges and greater refractive indices because of selenium's greater polarization. Thermoelectrically, rising electrical conductivity and moderate thermal conductivity with temperature lead to rising ZT values, which peak at 0.24 for ErSI and 0.22 for ErSeI at 650 K. ErSI exhibits improved electrical performance and magnetic anisotropy, whereas ErSeI has superior ductility, mechanical durability, and mobility-driven conductivity. The combination of mechanical, electronic, and thermoelectric properties emphasizes the materials' flexibility. ErSI and ErSeI are excellent choices for future incorporation into spintronic, optoelectronic, and energy conversion technologies due to their robust elastic response, semiconducting nature, and high-temperature thermoelectric efficiency.

Conflicts of interest

There are no conflicts to declare.

Data availability

Data are available upon request from the corresponding author.

Supplementary information is available. See DOI: **https://doi.org/10.1039/d5ra05496f**.

Acknowledgements

This work was supported and funded by the Deanship of Scientific Research at Imam Mohammad Ibn Saud Islamic University (IMSIU) (grant number IMSIU-DDRSP2503).

References

1 S. Johnsen, Z. Liu, J. A. Peters, J.-H. Song, S. Nguyen, C. D. Malliakas, H. Jin, A. J. Freeman, B. W. Wessels and M. G. Kanatzidis, *J. Am. Chem. Soc.*, 2011, **133**, 10030–10033.
2 A. Bouarissa, A. Gueddim, N. Bouarissa and H. Maghraoui-Meherezi, *J. Mater. Sci. Eng. B*, 2021, **263**, 114816.
3 A. Audzijonis, R. Sereika, V. Lapeika and R. Žaltauskas, *Phys. Status Solidi B*, 2007, **244**, 3260–3264.
4 A. Samavati, A. Awang, Z. Samavati, A. Fauzi Ismail, M. H. D. Othman, M. Velashjerdi, G. Eisaabadi B and A. Rostami, *J. Mater. Sci. Eng. B*, 2021, **263**, 114811.

5 K. Nejezchleb and J. Horák, *Czech. J. Phys.*, 1968, **18**, 138–142.
6 M. Nowak, P. Szperlich, Ł. Bober, J. Szala, G. Moskal and D. Stróż, *Ultrason. Sonochem.*, 2008, **15**, 709–716.
7 A. Audzijonis, L. Žigas, J. Siroic, A. Pauliukas, R. Žaltauskas, A. Čerškus and J. Narušis, *Phys. Status Solidi B*, 2006, **243**, 610–617.
8 X. Hu, X. Fan, B. Feng, D. Kong, P. Liu, C. Xu, Z. Kuang, G. Li and Y. Li, *J. Mater. Sci. Eng. B*, 2021, **263**, 114846.
9 A. Azam, N. Muhammad, G. Murtaza, N. Jafar, T. Alshahrani, M. A. Amin, M. Morsi, H. H. Somaily and Q. Mahmood, *Phys. Scr.*, 2022, **97**, 125806.
10 C. Tablero, *J. Alloys Compd.*, 2016, **678**, 18–22.
11 R. Nitsche and W. J. Merz, *J. Phys. Chem. Solids*, 1960, **13**, 154–155.
12 P. Kichambare, *Solid State Ionics*, 1997, **101–103**, 155–159.
13 D. Hajra, R. Sailus, M. Blei, K. Yumigeta, Y. Shen and S. Tongay, *ACS Nano*, 2020, **14**, 15626–15632.
14 X. Luo, L. Pan, T. Zhang, C.-E. Hu, Y. Cheng and H.-Y. Geng, *Mater. Sci. Semicond. Process.*, 2023, **166**, 107759.
15 Q. Cheng, L. Song, H. Lin, Y. Yang, Y. Huang, F. Su and T. Chen, *Langmuir*, 2019, **36**, 250–256.
16 O. V. Bokotey, *J. Alloys Compd.*, 2016, **678**, 444–447.
17 O. V. Bokotey, *Nanoscale Res. Lett.*, 2016, **11**, 251.
18 O. V. Bokotey, K. E. Glukhov, I. I. Nebola and A. A. Bokotey, *J. Alloys Compd.*, 2016, **669**, 161–166.
19 C. Nefzi, M. Souli, Y. Cuminal and N. Kamoun-Turki, *J. Mater. Sci. Eng. B*, 2020, **254**, 114509.
20 O. V. Bokotey, V. V. Vakulchak, I. I. Nebola and A. A. Bokotey, *J. Phys. Chem. Solids*, 2016, **99**, 153–158.
21 N. V. Pervukhina, V. I. Vasil'ev, S. A. Magarill, S. V. Borisov and D. Yu. Naumov, *Can. Mineral.*, 2006, **44**, 1247–1255.
22 Yu. V. Minets, Yu. V. Voroshilov and V. V. Pan'ko, *J. Alloys Compd.*, 2004, **367**, 109–114.
23 N. T. Hahn, S. Hoang, J. L. Self and C. B. Mullins, *ACS Nano*, 2012, **6**, 7712–7722.
24 N. T. Hahn, A. J. Rettie, S. K. Beal, R. R. Fullon and C. B. Mullins, *J. Phys. Chem. C*, 2012, **116**, 24878–24886.
25 A. M. Ganose, K. T. Butler, A. Walsh and D. O. Scanlon, *J. Mater. Chem. A*, 2016, **4**, 2060–2068.
26 H. Shi, W. Ming and M.-H. Du, *Phys. Rev. B*, 2016, **93**, 104108.
27 J. Di, J. Xia, H. Li, S. Guo and S. Dai, *Nano Energy*, 2017, **41**, 172–192.
28 J. Luitz, M. Maier, C. Hébert, P. Schattschneider, P. Blaha, K. Schwarz and B. Jouffrey, *Eur. Phys. J. B*, 2001, **21**, 363–367.
29 P. Blaha, K. Schwarz, F. Tran, R. Laskowski, G. K. Madsen and L. D. Marks, *J. Chem. Phys.*, 2020, **152**, 074101.
30 J. P. Perdew, K. Burke and M. Ernzerhof, *Phys. Rev. Lett.*, 1996, **77**, 3865–3868.
31 G. K. H. Madsen and D. J. Singh, *Comput. Phys. Commun.*, 2006, **175**, 67–71.
32 M. J. Varjovi, M. E. Kilic and E. Durgun, *Phys. Rev. Mater.*, 2022, **6**, 034004.
33 H. Koc, S. Palaz, A. M. Mamedov and E. Ozbay, *Ferroelectrics*, 2017, **511**, 22–34.
34 P. Chauhan and A. Kumar, *ACS Omega*, 2024, **9**, 33723–33734.
35 T. ÖZER, *Int. J. Adv. Eng. Pure Sci.*, 2023, **35**, 18–26.
36 T. Ozer and S. Cabuk, *J. Mol. Model.*, 2018, **24**, 66.
37 L. Rao, G. Tang and J. Hong, *Phys. Rev. Mater.*, 2023, **7**, 014010.
38 A. Bafekry, M. Faraji, M. M. Fadlallah, D. M. Hoat, H. R. Jappor, I. A. Sarsari, M. Ghergherehchi and S. A. Feghhi, *Phys. Chem. Chem. Phys.*, 2021, **23**, 25866–25876.
39 B. Peng, K. Xu, H. Zhang, Z. Ning, H. Shao, G. Ni, J. Li, Y. Zhu, H. Zhu and C. M. Soukoulis, *Adv. Theory Simul.*, 2018, **1**, 1700005.